Nanomanufacturing and Metrology (2025) 8:31
https://doi.org/10.1007/s41871-025-00278-5

ORIGINAL ARTICLE

Feedforward Compensation of Dynamics-Induced Form Errors in High-Speed Diamond Turning of Freeform Surfaces Using a Long-Stroke Fast Tool Servo

Takeshi Hashimoto[1] · **Jiwang Yan**[2]

Received: 27 April 2025 / Revised: 10 July 2025 / Accepted: 31 July 2025

Abstract

The fabrication of freeform optical components is increasingly demanded in emerging technologies such as augmented reality, imaging systems, and compact spectrometers. Fast-tool-servo (FTS) diamond turning has become a promising solution for high-speed, high-precision machining of such surfaces. However, achieving nanometric form accuracy remains challenging due to servo-induced dynamic errors, particularly overshoot and control delay. This study proposes a feedforward methodology to predict and compensate for dynamics-induced form errors in long-stroke FTS systems. By capturing FTS position signals and applying normalized cross-correlation (NCC) analysis, a repeatable motion error referred to as the time-shifted following error (TSFE) was identified through time delay compensation of the servo. The three-dimensional map of TSFE was constructed and integrated into the tool path to compensate for the error before machining. Experimental machining test of a dual-sinewave freeform shape achieved peak-to-valley (PV) form error of 0.26 μm, which was a 56% reduction compared to without measurement compensation. The repeatability of the three-dimensional map of TSFE showed a standard deviation of 0.007 μm on the PV, which confirmed that the TSFE map has enough repeatability to be used as a pre-compensation dataset. Additionally, the FTS system had latent TSFE error regardless the spindle rotation rates. In this study the TSFE map derivation of system indicated approximately 0.5 μm PV. These findings establish a fundamental and broadly applicable framework for improving form accuracy in high-speed freeform optics manufacturing using FTS, contributing to the advancement of ultra-precision machining technologies.

Highlights

1. A feedforward methodology was proposed to predict and compensate for form errors induced by servo dynamics.
2. The time-shifted following error (TSFE) was identified using normalized cross-correlation analysis of the captured fast tool servo (FTS) signals.
3. TSFE-based feedforward compensation reduced form error by 56% in freeform machining using a long-stroke FTS.

Keywords Freeform optics fabrication · Ultraprecision machining · Fast tool servo · Feedforward compensation · Form accuracy

✉ Jiwang Yan
yan@mech.keio.ac.jp

[1] School of Integrated Design Engineering, Graduate School of Science and Technology, Keio University, Yokohama 223-8522, Japan

[2] Department of Mechanical Engineering, Faculty of Science and Technology, Keio University, Yokohama 223-8522, Japan

1 Introduction

Recent advancements in optical technology have driven innovation across numerous industries, including space exploration [1], defense and security [2], autonomous vehicles [3], and consumer electronics such as wearable devices [4]. Optical components play a crucial role in these

Published online: 28 November 2025

applications, notably impacting system performance and enabling device miniaturization, directly influencing overall product capabilities [5]. A variety of optical surface geometries have been developed in recent years, with freeform surface design emerging as a key approach widely utilized in the for next-generation optical systems [6–8].

Among recent technological advancements, augmented reality (AR) and virtual reality (VR) headsets have emerged as rapidly evolving applications that demand high-performance, lightweight, and compact optical components to ensure an immersive user experience. However, current headset designs remain suboptimal, prompting continuous research into novel optical configurations, such as pancake lenses and polarization-based optical folding, which aim to reduce device size while enhancing visual clarity [9]. Additionally, various optical combiner technologies have been introduced to further minimize display compactness and expand the field of view. With the advancements of AR/VR optical systems, the demand for sophisticated freeform optical surfaces continues to grow. These surfaces enable optimization of the optical path, correction of higher-order aberrations, and enhancement of imaging performance, all while maintaining minimal thickness and weight, making them crucial for next-generation optical devices [10].

Optical freeform surface design, defined by its non-rotationally symmetric features, is typically represented through mathematical formulations such as *XY* polynomials for general off-axis systems [11], Zernike polynomials for circular apertures requiring complex wavefront correction [12], and Q-type polynomials for precise control of wavefront aberrations in specialized optical applications [13]. Unlike conventional optical designs that rely on spherical or aspherical surfaces, freeform optics provide enhanced design flexibility. They enable more effective aberration correction with fewer optical elements, broaden the field of view, and shorten the optical path. Consequently, freeform optical designs not only enhance overall optical performance but also support device miniaturization [14], driving their increasing adoption in advanced optical systems.

In the context of freeform optics applications, Shu et al. [15] proposed a compact, full-color augmented reality near-eye display system that uses a freeform relay configuration comprising four freeform optical elements. Beyond imaging systems, freeform optical designs have also played a crucial role in advancing analytical instruments such as spectrometers. For example, Reimers et al. [16] reported performance enhancements in the Offner–Chrisp imaging spectrometer through the integration of a freeform optical design based on low-order Zernike polynomials.

Despite remarkable progress in optical design, the fabrication of freeform surfaces for optical components remains a major manufacturing challenge. Conventional approaches often rely on multi-axis diamond machining techniques such as raster fly cutting, raster milling, and ruling [1, 17, 18]. More recently, advancements in diamond turning technology have led to the development of an alternative method based on synchronized motion control. This method integrates a position-controlled rotational spindle axis (*C*-axis) with linear axes—commonly referred to as the slow tool servo (STS) technique [19]. Chen et al. [20] demonstrated the effectiveness of STS machining for freeform surfaces, achieving a form accuracy of 0.85 μm peak-to-valley (PV) on a 20 mm × 18 mm optical component.

Alongside these technological advancements, fast tool servo (FTS) technology has emerged as a promising solution for the precise and efficient fabrication of freeform surfaces. Compared to the STS technique, FTS can reduce production time by a factor of 10–15 relative to STS [21].

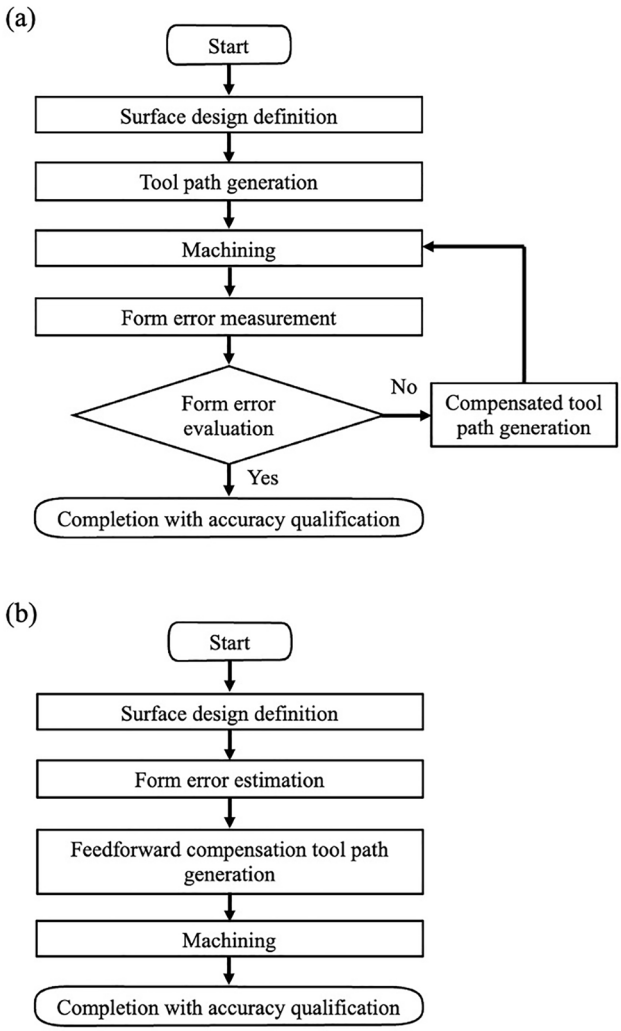

Fig. 1 **a** Conventional form error compensation process; **b** proposed feedforward compensation process

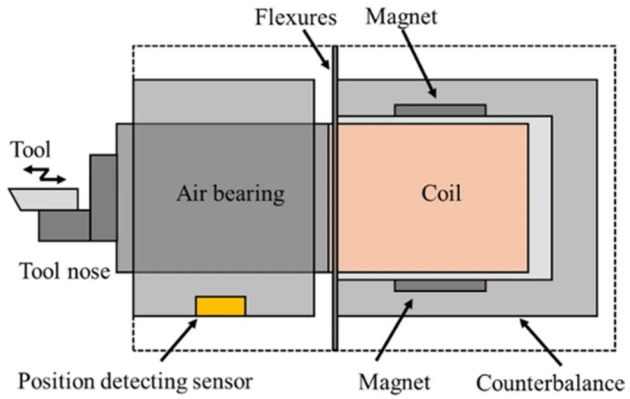

Fig. 2 Illustration of the FTS actuator

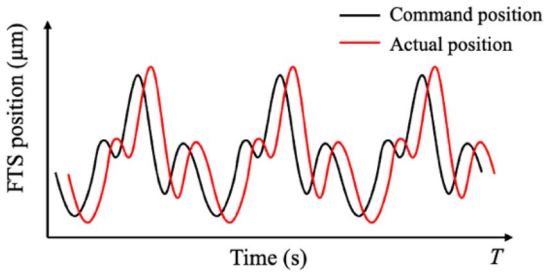

Fig. 4 Captured signal from FTS system

The integration of long-stroke FTS technology into diamond turning systems represents a key breakthrough in the fabrication of non-symmetrical freeform surfaces, offering substantial reductions in machining time while maintaining high precision [22]. However, one of the key challenges in these manufacturing methods is maintaining surface irregularity, commonly referred to as form error, within acceptable limits. Davis et al. [23] compared the relationship between machining efficiency and form accuracy across three fabrication methods: milling, STS, and FTS. Their results showed that FTS machining was approximately 10 times faster than STS; however, this increased speed came at the cost of approximately 20% higher form error compared to STS due to the faster machining conditions. Therefore, these results highlight the inherent tradeoff between machining efficiency and form accuracy. In contrast, recent demands from the optical manufacturing industry emphasize the need to achieve high precision and increased production efficiency.

In this study, to achieve high quality and machining efficiency simultaneously, a long-stroke FTS was employed for the fabrication of freeform surfaces via diamond turning, with particular focus on form errors originating from the FTS control mechanism. The dynamics-induced error of the FTS was identified by capturing and analyzing its position signals during operation. The extracted error pattern was then mapped in three dimensions and used as compensation data, which was applied in advance to the machining tool path through a feedforward compensation process. Consequently, the form accuracy of freeform surfaces fabricated using high-speed FTS machining notably improved in PV and root-mean-square (RMS) error compared to uncompensated results. This improvement demonstrates that servo-induced overshoot errors mostly contributed to form deviation. The repeatability of the servo-induced error was verified, confirming its suitability for use as correction data. This study establishes a predicative methodology for identifying and feedforward-compensating FTS-induced form errors, contributing to enhanced form accuracy in the high-speed production of freeform optics using independently controlled FTS systems.

2 Methodology

2.1 Concept of Feedforward Form Error Compensation

In conventional freeform machining processes, form error compensation is typically performed by using off-line form error measurements to generate an error-compensated tool path, which is then utilized in a subsequent machining

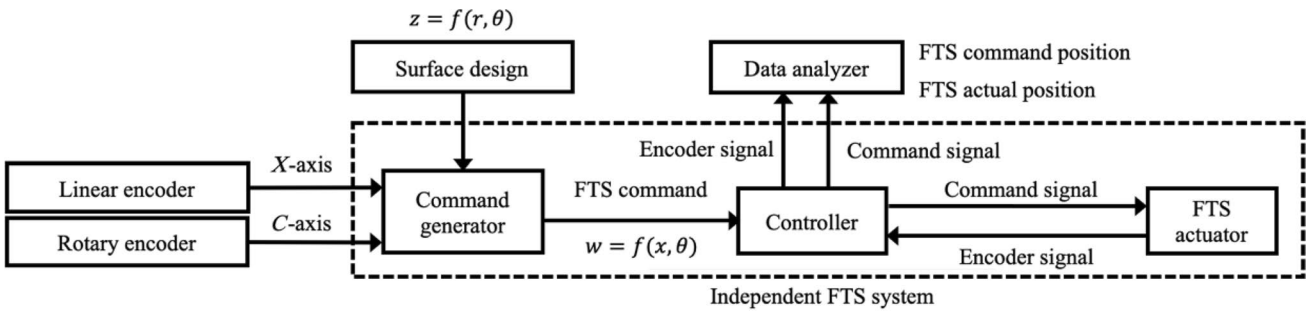

Fig. 3 Signal flow of the FTS system

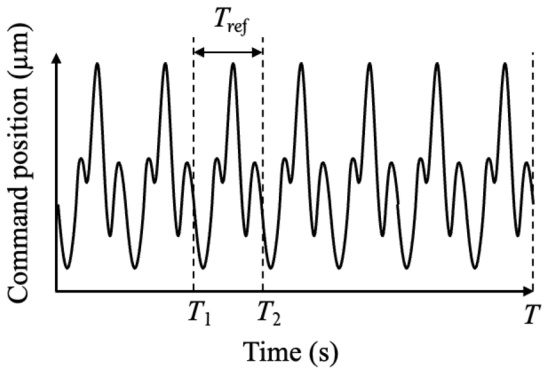

Fig. 5 Command position signal from the FTS system

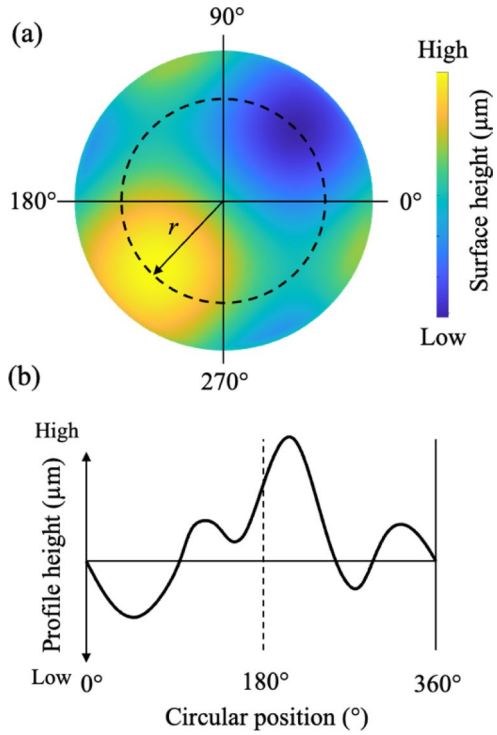

Fig. 6 **a** Design surface map; **b** surface profile at the radius *r*

process [24]. Liu et al. [25] proposed a method for machining freeform surfaces by applying form error compensation through Zernike polynomial fitting of raster measurement data obtained from an off-line measurement system. Figure 1a illustrates this conventional process, which begins with surface design definition, followed by tool path generation and initial machining. If the measured form error exceeds the specified tolerance, then additional compensation machining is performed based on the form error data. This iterative method is effective when the form error exhibits sufficient repeatability.

In such cases, once a repeatable error pattern is identified, compensation can be applied before machining, which is referred to as feedforward compensation. Figure 1b illustrates the process proposed in this study. Unlike the conventional approach, the proposed method predicts form error in advance based on known error characteristics and adjusts the tool path before the initial machining. This approach streamlines the overall process and enables the desired form accuracy to be achieved the need for post-machining error compensation based on form error measurements.

In the context of freeform diamond turning, Nagayama et al. [26] examined error estimation by analyzing its sources and applying compensation in STS machining of micrometer-scale freeform surfaces. They classified the error sources into three categories: program-related, tool-related, and process-related. While STS systems involve relatively slow tool motion, FTS systems operate at substantially higher speeds and with longer strokes, leading to more complex motion-control-induced form errors. Although previous studies [27, 28] have addressed time delay errors in high-speed FTS machining, residual form errors persist even after time delay compensation. This study focuses on analyzing these residual errors and developing methods for their compensation.

2.2 Machine Platform and FTS System

This study utilized an ultraprecision diamond-turning machine (Nanoform X, AMETEK Precitech Inc., USA) equipped with five-axis simultaneous control. The system features an air-bearing work spindle (*C*-axis), oil hydrostatic linear slides for the *X*-, *Y*-, and *Z*-axes, and a rotary *B*-axis table. All axes operate under closed-loop feedback control with picometer-level resolution. An independently controlled FTS (FTS5000, AMETEK Precitech Inc.) functions as the *W*-axis, enabling synchronized motion control based on encoder signals from the *X*- and *C*-axes.

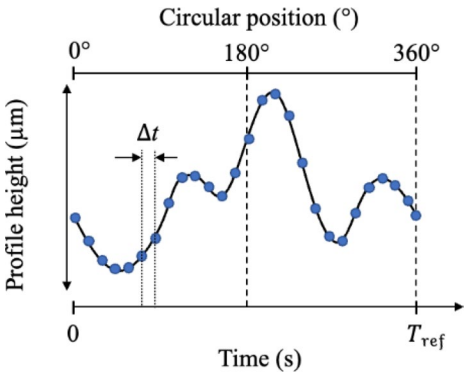

Fig. 7 Reference plot derived from the design surface

As shown in Fig. 2, the FTS actuator comprises an air-bearing piston with a full stroke of 5 mm. Position control is maintained via a closed-loop system using a glass-scale linear encoder with nanometer-level resolution. Driven by a voice coil motor and stabilized by a counterbalancing mass damper, the system supports sinusoidal motion with a 2000 μm amplitude at 100 Hz, achieving peak and continuous accelerations of 40 and 25 G, respectively [21].

2.3 Signal Acquisition and Processing Framework

The signal flow of the FTS system is illustrated in Fig. 3. Encoder signals from the linear (*X*-axis) and rotary (*C*-axis) of the machine platform are input to the FTS command generator, which calculates the *W*-axis (FTS) command position based on the part program. This *W*-axis command is then transmitted to an amplifier that drives the FTS actuator. Simultaneously, the actual position, measured by the internal glass-scale encoder, is fed back to the controller for closed-loop control. A data acquisition system records the command and actual position signals at a sampling frequency of 20 kHz over a 1.5-s duration. An example of the recorded signals is shown in Fig. 4, where a visible time delay between the command and actual position signals is evident, attributed to the dynamic response of the servo system.

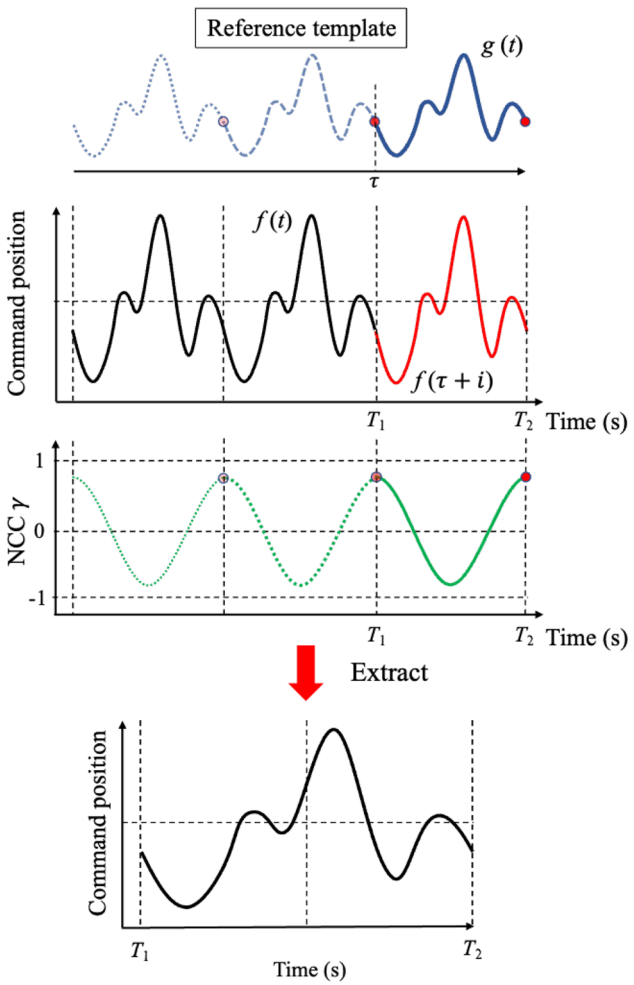

Fig. 8 Concept of extracting a single rotation profile using NCC

2.4 Time-Shifted Following Error (TSFE) Identification

Aiming to quantify the dynamic motion error of the FTS system, this study introduces a methodology based on normalized cross-correlation (NCC) to extract a full-rotation motion profile from the captured time-domain signal. The procedure involves four main stages.

2.4.1 Reference Profile Generation and Sampling Conditions

Figure 5 shows the FTS command signal captured during the machining process. The signal profile exhibits repeated surface deviations corresponding to each spindle rotation. Let T represent the total sampling duration, and T_{ref} denote the time for one full spindle rotation, defined as follows:

$$T_{\text{ref}} = \frac{60}{N} = T_2 - T_1, \tag{1}$$

where N is the spindle rotation rate in rpm. The start and end of a single rotation cycle are marked as T_1 and T_2, respectively.

Aiming to extract single-cycle information from the captured signal, this signal is compared to the corresponding design surface profile at the tool location during data sampling. Figure 6a illustrates an example of the design surface map, while Fig. 6b illustrates the surface plot over one full rotation at a distance r from the rotational center.

Aiming to precisely extract a single-cycle surface profile from a time-domain dataset obtained from the FTS system, this study employs a mathematical framework for signal pattern detection based on the NCC method. Commonly used in signal-processing, this approach enables accurate reconstruction of the original surface profile from repetitive measurements [29]. By quantitatively assessing the similarity between a known reference profile and the captured signal, comprising multiple rotations of the same surface, the proposed method allows for the reliable extraction of a representative circular profile embedded in the time-domain dataset.

First, the captured signal is sampled at the system's sampling frequency for the maximum sampling duration. The resulting dataset comprises discrete time-domain data, which can be described as follows:

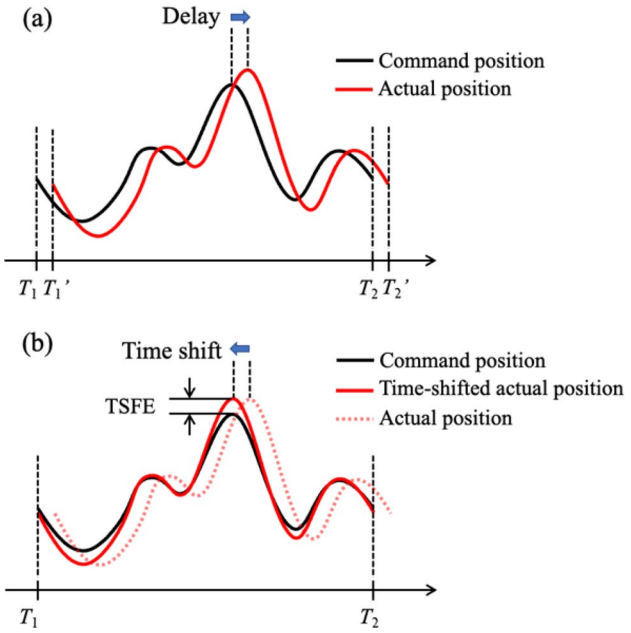

Fig. 9 **a** Captured raw signals from FTS after NCC extraction; **b** TSFE derivation through application of time delay compensation

$$f[n] = f(n \bullet \Delta t), n = 0,1,2,\ldots,M-1 \tag{2}$$

where M represents the total number of datasets, which is constrained by the system's capabilities. In this study, the data sampling frequency of the system was 20 kHz, and the maximum sampling time T was 1.5 s. Therefore, the maximum number of data points was limited to 30,000.

Second, the reference plot, which is derived from the design surface, shows the relationship between profile height and polar position, as shown in Fig. 7. Given the spindle rotation rate N, this reference plot can be converted from circular position information into time-domain information using Eq. (1). Thus, the time-domain representation of the reference plot is described using Eq. (3). This representation shares the same sampling time spacing as the FTS system Δt, as described in Fig. 7.

$$g[n] = g(n \bullet \Delta t), n = 0,1,2,\ldots,N-1 \tag{3}$$

The total number of datasets, N_d, in the reference profile is expressed using Eq. (4).

$$N_d = f_s \cdot T_{ref}, \tag{4}$$

where f_s is the sampling frequency, T_{ref} is the total reference period, and $\lfloor \cdot \rfloor$ denotes the floor function, which returns the largest integer less than or equal to its input.

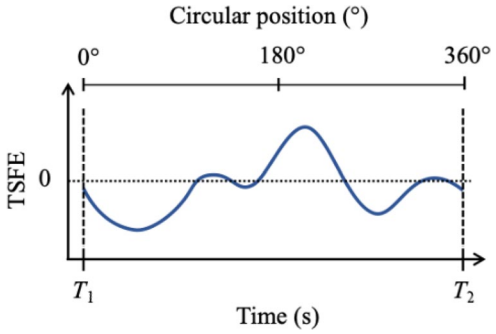

Fig. 10 TSFE profile

2.4.2 NCC-Based Cycle Pattern Detection

NCC is a widely used pattern-matching technique that measures the similarity between two discrete signals by sliding a reference signal along the target signal [30, 31]. Unlike standard correlation, NCC compensates for differences in mean and amplitude, ensuring the peak correlation value lies between − 1 and 1, which corresponds to the point where the signals are most closely aligned. In this study, NCC is applied to detect a single rotation profile within the captured FTS position signal. The reference profile, denoted as $g[n]$, is a known signal template derived from the designed surface profile at a specific radial distance, while the captured signal is denoted as $f[n]$. As illustrated in Fig. 8, the reference profile is shifted across the captured signal, with similarity evaluated at each shift. The NCC $\gamma(\tau\Delta t)$ at lag τ is computed as follows:

$$\gamma(\tau \cdot \Delta t) = \frac{\sum_{i=0}^{N-1}\left[f[\tau+i] - \langle f\rangle_\tau\right]\cdot\left[g[i] - \langle g\rangle\right]}{\sqrt{\left\{\sum_{i=0}^{N-1}\left[f[\tau+i] - \langle f\rangle_\tau\right]^2 \cdot \sum_{i=0}^{N-1}\left[g[i] - \langle g\rangle\right]^2\right\}}}, \tag{5}$$

$$\langle f\rangle_\tau = \frac{1}{N}\sum_{i=0}^{N-1} f(\tau+i), \tag{6}$$

$$\langle g\rangle = \frac{1}{N}\sum_{i=0}^{N-1} g(i), \tag{7}$$

where $f(t)$ represents the captured profile, and $g(t)$ denotes the reference profile generated from the circular plot at r of the surface. τ indicates the shift applied to the reference profile for calculating the NCC, and i is the index number of the data point. In this case, τ corresponds to the system's sampling rate of 50 µs. $\langle f\rangle_\tau$ refers to the mean value of the captured profile within the time window at τ, while $\langle g\rangle$ is the mean of the reference profile. The NCC function, denoted as γ, exhibits local maxima at points where the reference

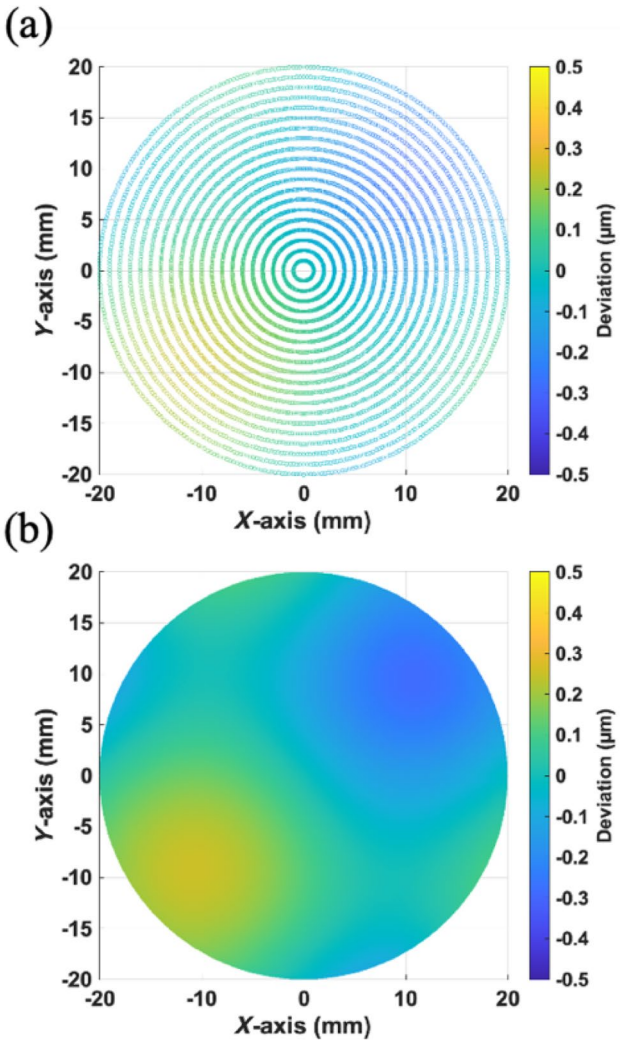

Fig. 11 **a** Raw TSFE map before interpolation, shown in circular coordinates. **b** Interpolated TSFE map in Cartesian coordinates for use in tool path compensation

signal closely matches segments of the captured signal. The maximum correlation value is defined as follows:

$$\gamma_{\max} = \max_{t} \gamma(\tau \cdot \Delta t), \tag{8}$$

where $\tau\Delta t$ is equivalent to the time at the maximum correlation value. Therefore, T_1 and T_2 can be expressed as follows:

$$T_1 = \tau \cdot \Delta t, \tag{9}$$

$$T_2 = T_1 + T_{\text{ref}}. \tag{10}$$

These peaks indicate the starting points of repeated cycles within the captured dataset. The FTS command signal involves multiple surface rotations; thus, several peaks are typically observed. For this study, a single rotation segment was selected arbitrarily for further analysis. As shown in Fig. 8, the extracted segment begins at time T_1 and ends at T_2, representing one complete rotation cycle of the tool path.

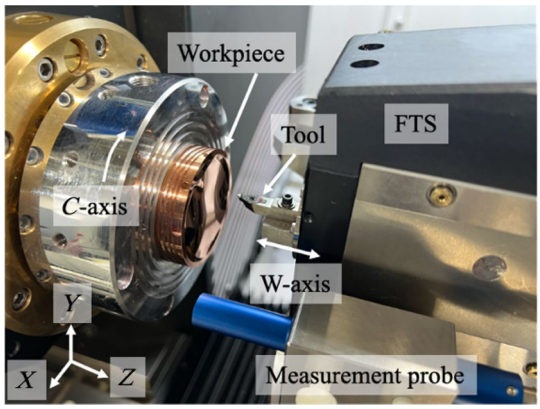

Fig. 12 Machine setup

2.4.3 TSFE Derivation Through Time Delay Compensation

After identifying the cycle start and end times (T_1, T_2) in Sect. 2.4.2, a single rotation segment of the FTS command signal is precisely extracted for further analysis. Simultaneously, the actual position signal is recorded using the data acquisition system, allowing for a direct comparison with the command trajectory. As illustrated in Fig. 9a, the extracted signals include the commanded and actual position profiles. A noticeable shift between these profiles is observed, caused by the inherent servo response delay in the FTS control system. This delay aligns with behaviors reported in previous studies, where methods for time delay identification and correction were proposed and subsequently applied in this study [28].

Aiming to compensate for this delay, the actual position profile is shifted backward by the calculated time delay, as illustrated in Fig. 9b. This adjustment brings the actual motion into close alignment with the intended command signal. After compensation, the corrected actual position and the original commands are overlaid, demonstrating strong agreement in their shapes.

Finally, the TSFE is defined as the pointwise difference between the commanded profile and the time-shifted actual profile.

$$\text{TSFE}[n] = f_{\text{act}}[n - \delta] - f_{\text{cmd}}[n], \tag{11}$$

where f_{cmd} is the command position profile, f_{act} is the actual position profile, and δ is the calculated time delay in the profile.

Table 1 Freeform design shape information

Design information	Value
Surface design	Dual sinewave freeform
Diameter (mm)	40
Wavelength (mm)	40
Amplitude (mm)	0.75
Maximum sagitta (mm)	3.0
Maximum concentric slope (°)	9.45
Workpiece material	Oxygen-free copper

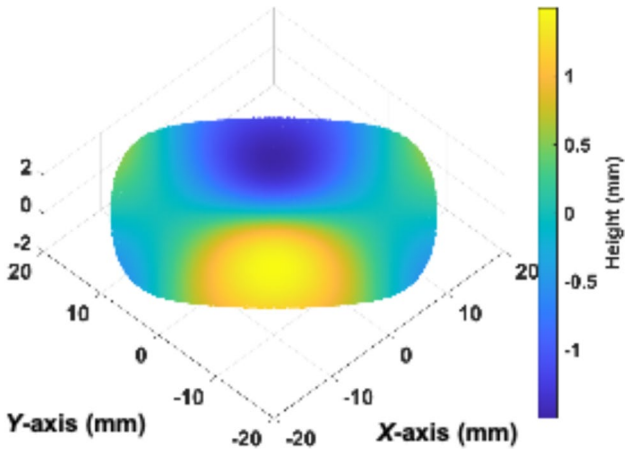

Fig. 13 Design surface map

The TSFE represents the dynamic motion error component of the FTS system. This error is derived by extracting a single-rotation profile and compensating for the time delay. This correction process effectively isolates overshoot behavior by eliminating the influence of servo lag. The resulting error profile captures transient effects intrinsic to high-speed tool motion, particularly during rapid direction changes in FTS-based machining. As shown in Fig. 10, the extracted TSFE profile clearly reveals the overshoot behavior, independent of any time delay effects.

2.5 TSFE Mapping and Tool Path Compensation

Aiming to generate a spatial TSFE map, the command and actual position signals are recorded at 1 mm radial intervals across the workpiece surface. At each radial position, a single-rotation profile is extracted and aligned following the procedures outlined in Sects. 2.4.2 and 2.4.3. The TSFE values are then calculated as pointwise differences between the commanded and time-shifted actual profiles. These profiles are then assembled along the radial direction to construct a coarse three-dimensional surface over a two-dimensional spatial domain, where the surface height represents the magnitude of dynamic error. Aiming to create a continuous surface suitable for tool path correction, the discrete data are interpolated onto a uniform Cartesian grid using cubic spline interpolation. Although the data are sampled at radial intervals of 1 mm, which is relatively coarse, the dynamic error amplitudes are typically only a few micrometers. Given that the TSFE surface spans a 40 mm diameter area, the resulting shape is extremely shallow, and the interpolation errors are negligible compared to the actual surface deviations. Moreover, cubic spline interpolation offers smoother transitions between points than linear interpolation, making it particularly beneficial for generating smooth and accurate tool paths. Therefore, this method was selected to reconstruct the continuous TSFE surface from the discrete data.

Table 2 Cutting conditions

Cutting conditions	Value
Tool material	Single-crystal diamond
Nose radius (mm)	0.50
Rake angle (°)	0
Clearance angle (°)	15
Spindle rotation rate (rpm)	1000
Feed rate (mm/min)	Rough: 10
	Finish: 2
Depth of cut (μm)	Rough: 10
	Finish: 2
Coolant	Oil mist
Machining time (min)	10

The generated TSFE map is visualized in Fig. 11a, showing the spatial distribution of dynamic motion errors in circular coordinates. After interpolation, the continuous TSFE surface is shown in Fig. 11b, converted to Cartesian coordinates for use in tool path correction.

The interpolated TSFE map is then incorporated into the compensated tool path using CAM software (Diffsys, AMETEK Precitech Inc). A modified point cloud is then generated based on the original design surface, the tool geometry, and the corresponding TSFE compensation values This updated tool path is used in subsequent machining operations, allowing form errors to be reduced by proactively accounting for deviations introduced by the FTS system.

3 Experimental Setup

3.1 Machine Configuration

The experimental setup is illustrated in Fig. 12. The FTS, functioning as the *W*-axis, is mounted on the *B*-axis and aligned parallel to the *Z*-axis. A diamond-turning tool is

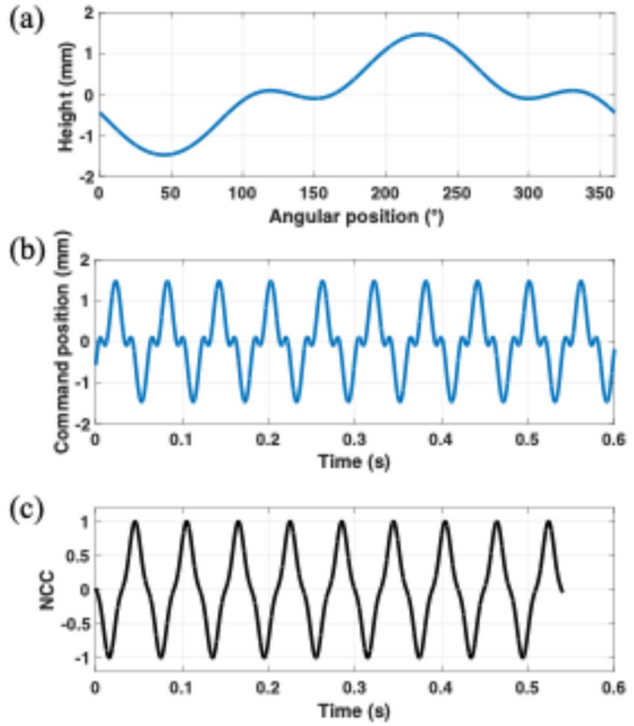

Fig. 14 TSFE derivation process using the NCC method: **a** Extracted circumferential profile at a radial distance of 16 mm, serving as the reference profile; **b** acquired signal from the FTS system over a 0.6 s interval; **c** NCC calculation result obtained by correlating the reference profile with the acquired profile

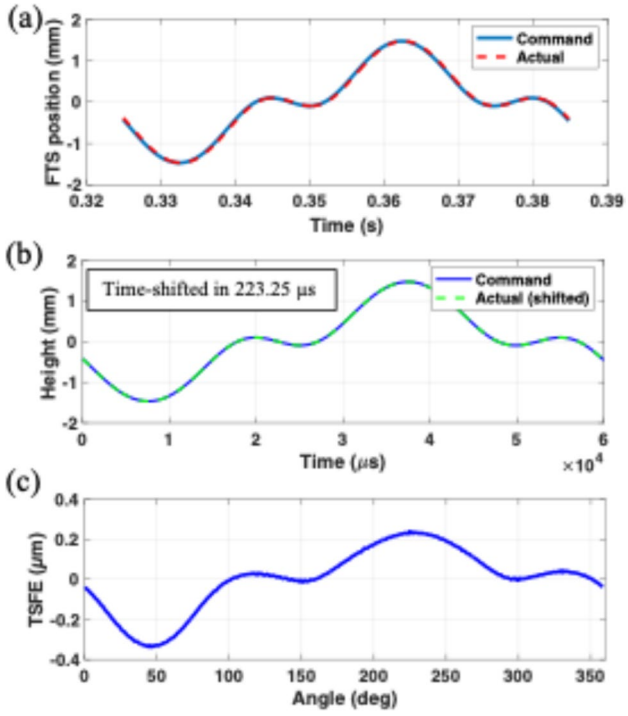

Fig. 15 TSFE derivation results: **a** Comparison of the FTS command profile and the actual profile within a single extracted cycle in the time domain; **b** comparison between the FTS command profile and the time-shifted actual profile (shifted by 223.25 μs) within one extracted cycle; **c** TSFE profile plotted over one full spindle rotation in the angular domain at a radial distance of 16 mm

installed at the tip of the FTS actuator. Aiming to enable on-machine sample alignment, a chromatic confocal optical probe is mounted adjacent to the FTS on the same *B*-axis platform. This configuration enables direct measurement of the clocking angle error immediately after machining, without removing the workpiece from the vacuum chuck. The workpiece is secured to the *C*-axis spindle using a vacuum chuck. A reference flat is included on the workpiece surface for alignment and is registered with the *C*-axis and *W*-axis zero positions of the machine to ensure consistent setup and traceable tool-path calibration.

3.2 Metrology System

A non-contact chromatic confocal optical probe (CHRocodile 2S, Precitec GmbH) was integrated into the machine setup for precise workpiece alignment. This probe employs chromatic confocal sensing technology, offering nanometer-scale axial resolution and high-speed data acquisition rates up to 10 kHz [32]. The measurement data from the probe are synchronized with encoder signals from the *X*-, *Y*-, *Z*-, and *C*-axes, enabling surface height to be captured as discrete points within the coordinate system of the machine. For post-process validation of form accuracy, an ultraprecision contact profilometer (UA3P, Panasonic) was used to conduct offline, full-surface measurements via raster scanning. Aiming to assess form error with high precision, the discrete measurement dataset was fitted to a 169-term Zernike polynomial, producing a continuous surface representation. This approach effectively reduced measurement noise and generated a smooth residual error map.

3.3 Test Shape Design

The test shape was defined using a combination of two orthogonal sinusoidal functions along the *X*- and *Y*-axes:

$$z(x,y) = A \bullet \left\{ \sin\left(\frac{2\pi x}{f_x}\right) + \sin\left(\frac{2\pi y}{f_y}\right) \right\}, \tag{12}$$

where A is the amplitude of the sinewave, while f_x and f_y are the wavelengths along the *X*- and *Y*-axes, respectively. In this study, these parameters were set as follows: $A = 0.75$ mm, and $f_x = f_y = 40$ mm, corresponding to the dual sinewave design outlined in Table 1. The surface representation based on these design parameters is shown in Fig. 13.

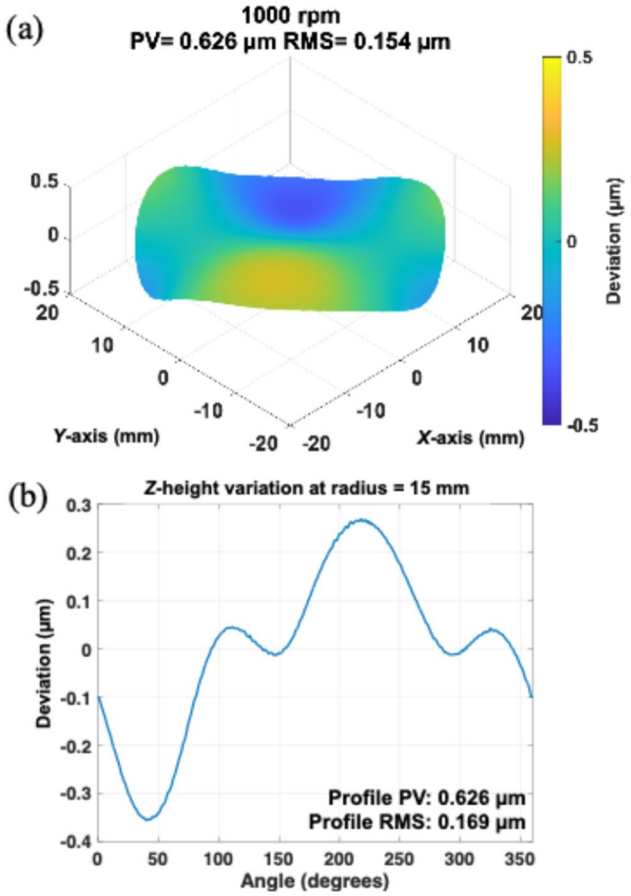

Fig. 16 **a** TSFE error map obtained at a spindle speed of 1000 rpm **b** TSFE extracted profile at 15 mm away from the rotational center

3.4 Experimental Conditions

Oxygen-free copper was selected as the workpiece material to reduce form errors caused by tool wear during testing. A single-crystal diamond tool, featuring a nose radius of 0.50 mm, a rake angle of 0°, and a clearance angle of 15°, was employed to prevent interference between the tool's clearance face and the machined surface. Aiming to generate the tool path, the designed surface and the tool geometry (as listed in Table 2) were first imported into CAM software. The surface produced tool path information in polar coordinates, optimized for the FTS system. Once the FTS system received and compiled the point-based tool path data, it computed the corresponding *W*-axis command positions in real time. Aiming to ensure smooth and continuous motion, the FTS system applied spline interpolation to the discrete *W*-axis points. These interpolated *W*-axis positions were then executed at a 20 kHz update rate, synchronized with the *C*-axis position. Although the tool path was not explicitly designed as a spiral trajectory, the real-time synchronization between the *C*-axis spindle and *W*-axis actuation produced a spiral-like cutting trajectory on the workpiece surface. The cutting conditions used in the experiment are summarized in Table 2. In this experiment, for the finish path, the spindle rotation rate was set to 1000 rpm, with a feed rate of 2 mm/min and a depth of cut of 2 μm. The total machining time for the finish path was approximately 10 min.

4 Results and Discussion

4.1 TSFE Profile Derivation

A surface profile along the circumferential direction of the design surface was first extracted. As an example, the profile at a radial distance of 16 mm was selected, as illustrated in Fig. 14a. This profile serves as the reference and corresponds to $g(t)$ in Fig. 8. Subsequently, the FTS command signal was recorded and analyzed at the same radial position ($r = 16$ mm) under the cutting conditions summarized in Table 2, ensuring direct comparison with the reference profile. The recorded signal is presented in Fig. 14b. Data extraction was performed over a 0.6 s interval, which corresponds to 10 spindle rotations.

Aiming to isolate a single rotation cycle from the acquired data, the NCC method was applied, following the procedure shown in Fig. 8. This procedure identified the start and end times of one full rotation cycle, denoted as T_1 and T_2, respectively, as described in Fig. 14c. The command and actual profiles for this extracted cycle are shown in Fig. 15a. In Fig. 15b, the command profile is shown alongside the actual profile, which has been temporally shifted by 223.25 μs, as determined using the time delay identification method [31]. Using the result shown in Fig. 15b and Eq. (11), the TSFE was applied. Finally, based on a spindle rotation rate of 1000 rpm, the TSFE profile representing one complete rotation in the circumferential direction at this radial location is presented in Fig. 15c.

4.2 TSFE-Based Error Map

Aiming to generate a three-dimensional TSFE map, the TSFE calculation described in Sect. 4.1 was applied at 1 mm radial intervals across the workpiece surface. The resulting TSFE-based error mapping is shown in Fig. 16a. Under the cutting conditions listed in Table 2, with a spindle speed of 1000 rpm, the PV magnitude of the TSFE error was measured at 0.626 μm. The spatial distribution of the TSFE closely resembled the nominal surface design, indicating that the primary source of error was the overshoot behavior of the servo control system. Notably, TSFE is calculated as the difference between the FTS command signal and the time-shifted actual position signal, both of which are directly recorded from the control system. Therefore, static tool alignment errors and geometric offsets are inherently

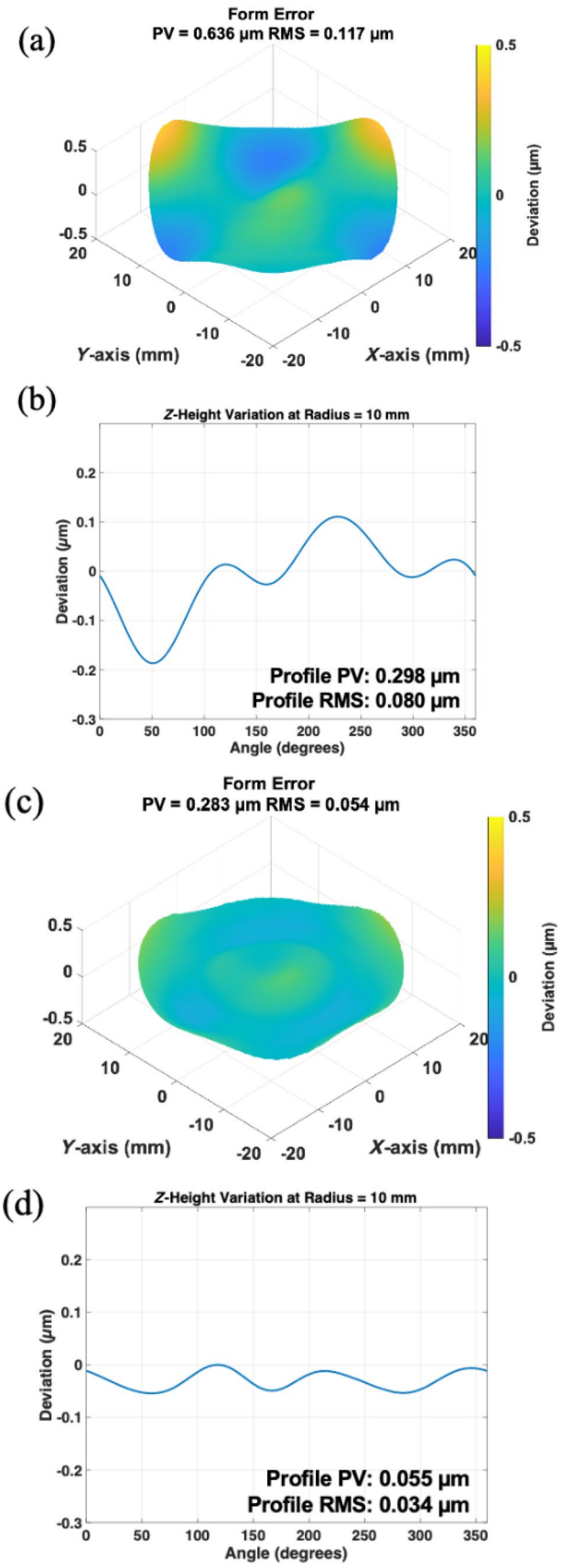

Fig. 17 **a** Measured form error before TSFE compensation. **b** Circumferential profile at 10 mm before compensation. **c** Form error after TSFE compensation. **d** Circumferential profile at 10 mm after compensation

excluded from this analysis. This exclusion ensures that the calculated TSFE reflects only the dynamic error characteristics of the FTS during the machining process. Figure 16b presents the TSFE profile over one spindle rotation, extracted at a radial distance of 15 mm from the spindle center. Although the error magnitude remains within the sub-micron range, a PV deviation of 0.626 μm is crucial in the context of ultraprecision optical components, where form accuracy requirements, such as for aspheric glass lenses used in imaging optics, generally fall within the 100 to 300 nm PV range [5].

4.3 Form Error Comparison Before/After Compensation

Figure 17a illustrates the form error of the machined surface prior to applying the TSFE compensation process. The form error was measured using an ultraprecision three-dimensional profiler with a raster scanning method. A 169-term Zernike polynomial fit was applied to the data, resulting in a PV form error of 0.636 μm and an RMS value of 0.117 μm. These values closely matched those obtained from the TSFE error map, and the spatial distribution of the errors exhibited a similar pattern. The circumferential profile extracted at a radial distance of 10 mm (Fig. 17b) revealed a PV deviation of 0.298 μm and an RMS of 0.080 μm before compensation. However, slight discrepancies were observed, possibly due to a minor residual tool alignment error that affected the observed surface shape.

In contrast, Fig. 17c presents the form error after applying the TSFE compensation process. The PV form error was substantially reduced to 0.283 μm, and the RMS value decreased to 0.054 μm, representing improvements of 56% and 54%, respectively. This finding confirms the effectiveness of the TSFE compensation approach. The circumferential profile at the same 10 mm radius after compensation (Fig. 17d) demonstrated further improvement, with the PV and RMS values reduced to 0.055 and 0.034 μm, respectively, confirming the localized effectiveness of the TSFE correction process. These results validate that FTS-induced dynamic errors are the primary contributors to form deviation in high-speed freeform machining. During the compensated machining, tool alignment was carefully controlled to minimize residual errors. However, a slight residual alignment error may still have influenced the final surface profile. The appearance of the machined freeform surface is shown in Fig. 18.

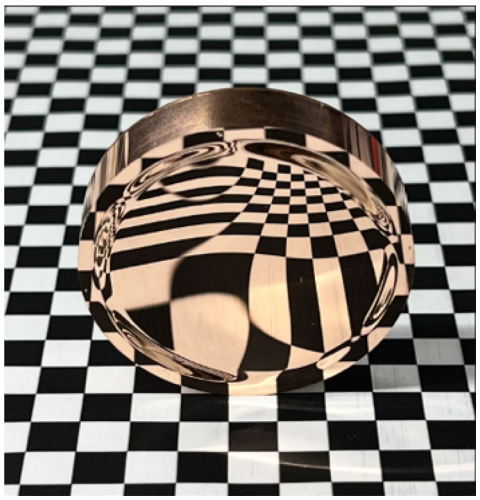

Fig. 18 Photograph of the machined freeform surface

Table 3 Result of the TSFE repeatability test

Test number	PV (μm)	RMS (μm)
1	0.626	0.154
2	0.636	0.155
3	0.625	0.154
4	0.641	0.155
5	0.621	0.152
Average	0.630	0.154
Difference	0.020	0.003
Standard deviation	0.008	0.001

Table 4 TSFE analysis result under different spindle rotation rates

Spindle rotation rate (rpm)	PV (μm)	RMS (μm)
500	0.539	0.136
750	0.566	0.141
1000	0.625	0.153
Difference	0.087	0.017

4.4 TSFE Repeatability

The PV values obtained from five repeated tests are summarized in Table 3. These experiments were conducted to evaluate the repeatability of the TSFE mapping process. The results showed excellent consistency, with a maximum PV difference of only 0.020 μm and a standard deviation of 0.008 μm. RMS values showed similarly low variation, with a maximum difference of 0.003 μm and a standard deviation of 0.001 μm. These results indicate that TSFE behavior is highly repeatable under consistent machining conditions. As discussed in Sect. 4.3, the TSFE-based compensation effectively corrected form errors, reducing them by approximately 56%, thereby confirming that FTS-induced dynamics are the dominant contributors. Therefore, the repeatability of TSFE mapping also indicates that the resulting form

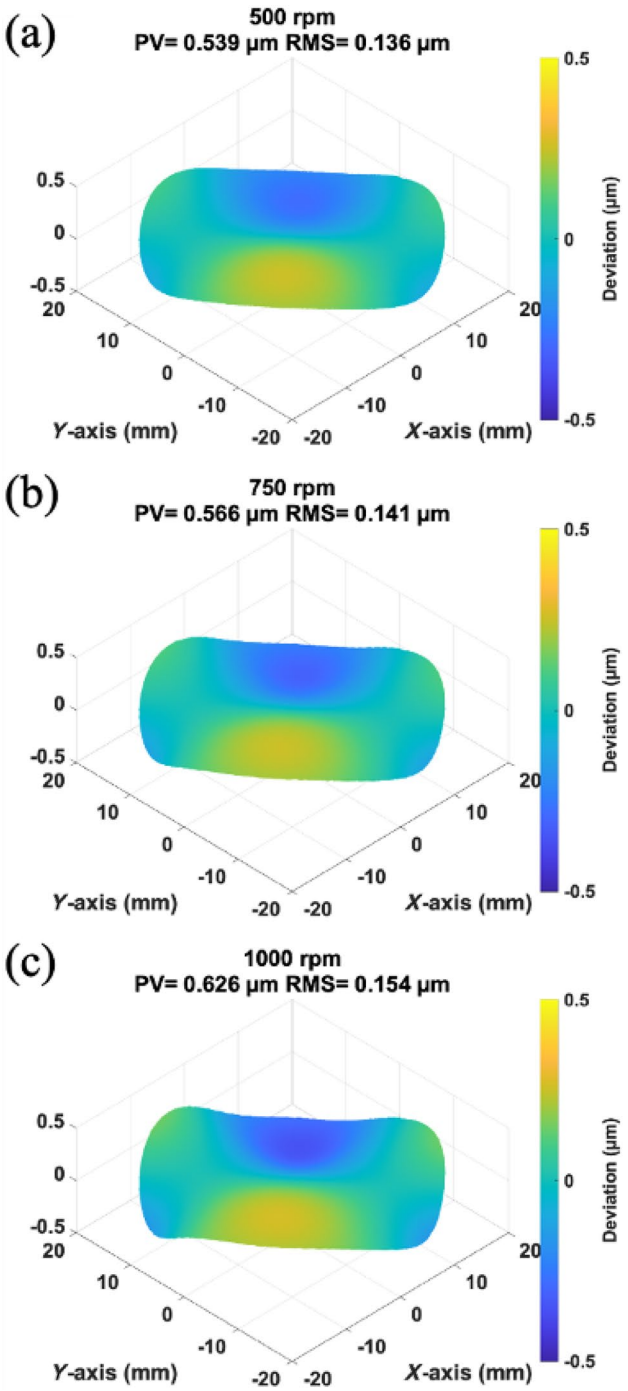

Fig. 19 Comparison of the TSFE map appearance between the spindle rotation rates: **a** 500 rpm, **b** 750 rpm, and **c** 1000 rpm

accuracy of the machining process should be reliably maintained across repeated operations.

4.5 Relationship Between the Spindle Rotation Rate and the TSFE

In this process, the spindle rotation is generally regarded as the most impactful parameter. This consideration is attributed to higher spindle rotation rates, which require more aggressive FTS reciprocation, altering the dynamic behavior of the system. Aiming to investigate the influence of spindle rotation rate on the characteristics of TSFE, a series of calculations were conducted using different spindle rotation rates. The workpiece shape used for these evaluations was the same dual sine wave shape described in Table 1. TSFE was evaluated at spindle speeds of 500, 750, and 1000 rpm, and the results are summarized in Table 4 and illustrated in Fig. 19a, b and c, respectively. The results show a slight increase in TSFE magnitude with rising spindle speed. Specifically, the PV value increased from 0.539 µm at 500 rpm to 0.626 µm at 1000 rpm, while the RMS value increased from 0.136 to 0.154 µm. However, the absolute differences in PV (0.087 µm) and RMS (0.017 µm) were relatively small. These results indicate that, within the tested range of 500 to 1000 rpm, typical for high-speed machining in ultraprecision freeform generation using FTS systems, the spindle rotation rate has only a limited influence on TSFE magnitude. Therefore, spindle rotation rate was not identified as a dominant factor influencing TSFE behavior in this study. Moreover, even at the lowest speed of 500 rpm, the form error PV still remained above 0.5 µm PV. This finding indicates that the FTS machining process inherently produces a certain latent TSFE pattern similar to the design shape, which contributes to the form error, regardless of spindle rotation rate. In this study, the observed TSFE map showed a PV of approximately 0.5 µm and a shape similar to the design form. Therefore, a latent error of at least 0.5 µm PV existed in this system, regardless of the spindle rotation rate. Selecting a representative spindle rotation rate within a practical range is good practice to estimate the form error and effectively understand the FTS behavior relative to the required surface shape.

5 Conclusion

This study explored dynamics-induced form errors in FTS-based diamond turning of freeform optical surfaces and proposed a feedforward compensation strategy aimed at eliminating servo-related motion errors. Based on the results, the following conclusions were drawn:

a) By comparing the extracted circular profile from the designed shape with the captured position signals from the FTS system using a normalized cross-correlation (NCC) process, a one-rotation signal could be systematically extracted and effectively used for analyzing servo-induced errors.
b) The extracted profiles were further analyzed using a time delay cancellation process to identify the TSFE, representing the overshoot behavior of the servo system. A three-dimensional data map of the TSFE profile enabled estimation of the form error in high-speed freeform machining.
c) This TSFE-based error map was then applied as a feedforward compensation estimation map. With TSFE compensation, the resulting form error in high-speed freeform machining was reduced to 0.26 µm PV and 0.01 µm RMS, representing 56% and 54% reductions, respectively, compared to results without compensation.
d) The repeatability of the TSFE mapping was confirmed through testing, revealing a standard deviation of only 0.008 µm in the TSFE PV value. This high level of repeatability indicates that the machining process, when using TSFE-based error compensation, consistently maintains improved form accuracy.
e) Analysis of the relationship between spindle rotation rate and TSFE showed that spindle rotation rate was not a dominant influencing factor on TSFE behavior. This result implies that the form error in FTS machining tends to follow a consistent, latent TSFE map similar to the design shape, regardless of the spindle rotation rate. In this study, the form error PV for the given design was 0.539 µm at 500 rpm and 0.625 µm at 1000 rpm, indicating a latent TSFE error of approximately 0.5 µm PV.

These findings demonstrate the feasibility and effectiveness of a dynamics-based feedforward error compensation methodology for ultraprecision freeform machining using long-stroke FTS systems. Although the quantitative results are specific to the system used, the TSFE-based framework offers a generally applicable basis for improving form accuracy and machining efficiency in various FTS-based manufacturing platforms.

Acknowledgements The authors would like to extend thanks to AMETEK Precitech Inc., USA, for providing technical support and information on the ultraprecision diamond turning machine and the fast tool servo system used in this study. This work has been partially supported by Japan Society for the Promotion of Science under the Grant-in-Aid for Scientific Research (A), project number 25H00709.

Author contributions All authors read and approved the final manuscript.

Funding Japan Society for the Promotion of Science London, 25H00709, Jiwang Yan.

Data Availability No data are associated with the manuscript.

Declarations

Competing Interests Prof. Jiwang Yan is an editorial board member for "Nanomanufacturing and Metrology" and was not involved in the editorial review, or the decision to publish this article. The authors declare that they have no known competing financial interests or personal relationships that could have appeared to influence the work reported in this paper.

References

1. Xie Y, Mao X, Li J, Wang F, Wang P, Gao R, Li X, Ren S, Xu Z, Dong R (2020) Optical design and fabrication of an all-aluminum unobscured two-mirror freeform imaging telescope. Appl Opt 59(3):833–840. https://doi.org/10.1364/AO.379324
2. Kress B, Starner T (2013) A review of head-mounted displays (HMD) technologies and applications for consumer electronics. Proc SPIE 8720:87200A. https://doi.org/10.1117/12.2015654
3. Li Z, Fang F, Chen J, Zhang X (2017) Machining approach of freeform optics on infrared materials via ultra-precision turning. Opt Express 25(3):2051–2063. https://doi.org/10.1364/OE.25.002051
4. Chang C-M, Shieh H-PD (2000) Design of illumination and projection optics for projectors with single digital micromirror devices. Appl Opt 39(19):3202–3208. https://doi.org/10.1364/AO.39.003202
5. Yin S, Jia H, Zhang G, Chen F, Zhu K (2017) Review of small aspheric glass lens molding technologies. Front Mech Eng 12(1):66–76. https://doi.org/10.1007/s11465-017-0417-2
6. Rolland JP, Davies MA, Suleski TJ, Evans C, Bauer A, Lambropoulos JC, Falaggis K (2021) Freeform optics for imaging. Optica 8(2):161–182. https://doi.org/10.1364/OPTICA.413762
7. Fang FZ, Zhang XD, Weckenmann A, Zhang GX, Evans C (2013) Manufacturing and measurement of freeform optics. CIRP Ann-Manuf Technol 62(2):823–846. https://doi.org/10.1016/j.cirp.2013.05.003
8. Garrard K, Bruegge T, Hoffman J, Dow T, Sohn A (2005) Design tools for freeform optics. Proc SPIE 5874:58740A. https://doi.org/10.1117/12.618165
9. Cakmakci O, Qin Y, Bosel P, Wetzstein G (2021) Holographic pancake optics for thin and lightweight optical see-through augmented reality. Opt Express 29(22):35206–35215. https://doi.org/10.1364/OE.439585
10. Maimone A, Wang J (2020) Holographic optics for thin and lightweight virtual reality. ACM Transactions on Graphics (TOG) 39(4):67. https://doi.org/10.1145/3386569.3392416
11. Moein S, Suleski TJ (2021) Freeform optics for variable extended depth of field imaging. Opt Express 29(24):40524–40537. https://doi.org/10.1364/OE.439980
12. Niu K, Tian C (2022) Zernike polynomials and their applications. J Opt 24(12):123001. https://doi.org/10.1088/2040-8986/ac9e08
13. Murray IB (2017) Optimizing reflective systems using aspheric and freeform surfaces. Opt Soc America. https://doi.org/10.1364/IODC.2017.JTu1C.6
14. Narasimhan BA (2018) Ultra-compact pancake optics based on ThinEyes® super-resolution technology for virtual reality headsets. Proc SPIE 10676:106761G. https://doi.org/10.1117/12.2315688
15. Shu T, Hu G, Wu R, Li H, Zhang Z, Liu X (2022) Compact full-color augmented reality near-eye display using freeform optics and a holographic optical combiner. Opt Express 30(18):31714–31726. https://doi.org/10.1364/OE.465842
16. Reimers J, Bauer A, Thompson KP, Rolland JP (2017) Freeform spectrometer enabling increased compactness. Light Sci Appl 6:e17026. https://doi.org/10.1038/lsa.2017.26
17. Brinksmeier E, Gläbe R, Schönemann L (2012) Review on diamond-machining processes for the generation of functional surface structures. CIRP J Manuf Sci Technol 5(1):1–7. https://doi.org/10.1016/j.cirpj.2011.10.003
18. Smilie PJ, Dutterer BS, Lineberger JL, Davies MA, Suleski TJ (2011) Freeform micromachining of an infrared Alvarez lens. Proc SPIE 7927:79270K. https://doi.org/10.1117/12.876159
19. Mishra V, Burada DR, Pant KK, Karar V, Jha S, Khan GS (2019) Form error compensation in the slow tool servo machining of freeform optics. Int J Adv Manuf Technol 105:1623–1635. https://doi.org/10.1007/s00170-019-04359-w
20. Chen CC, Huang CY, Peng WJ, Cheng YC, Yu ZR, Hsu WY (2013) Freeform surface machining error compensation method for ultra-precision slow tool servo diamond turning. Proc SPIE 8838:88380Y. https://doi.org/10.1117/12.2022981
21. AMETEK Precitech Inc (2025) FTS5000, https://www.precitech.com/product/accessoriesoverview/fasttoolservo/. [Accessed 1 Mar 2025].
22. He K, Dai Y, Guan C, Tie G, Hu H (2018) High-frequency precision motion control of fast axis servo device. Proc SPIE 10838:1083809. https://doi.org/10.1117/12.2504806
23. Davis GE, Roblee JW, Hedges AR (2009) Comparison of freeform manufacturing techniques in the production of monolithic lens arrays. Proc SPIE 7426:742605. https://doi.org/10.1117/12.824451
24. Yu S, Wang Y, Yao P, Wang H, Liu Z, Jin X, Liu C, Bao X, Chu D, Qu S, Huang C (2023) A novel machining approach of freeform multi-mirror mold via normal swing cutting. J Manuf Process 94:316–327. https://doi.org/10.1016/j.jmapro.2023.03.066
25. Liu J, Zhao Y, Liu K, Wang L, Li F (2023) Compensation machining of freeform based on fast tool servo system. PLoS ONE 18(3):e0282752. https://doi.org/10.1371/journal.pone.0282752
26. Nagayama K, Yan J (2021) Deterministic error compensation for slow tool servo-driven diamond turning of freeform surface with nanometric form accuracy. J Manuf Process 64:45–57. https://doi.org/10.1016/j.jmapro.2021.01.015
27. Tanikawa S, Sato Y, Yan J (2023) A novel calibration method for angular misalignment in independently controlled fast tool servo-based diamond turning. Precis Eng 83:216–227. https://doi.org/10.1016/j.precisioneng.2023.06.010
28. Hashimoto T, Yan J (2025) Time delay compensation in high-speed diamond turning of freeform surface using independent fast tool servo with a long stroke. Precis Eng 93:515–527. https://doi.org/10.1016/j.precisioneng.2025.02.006

29. Briechle K, Hanebeck UD (2001) Template matching using fast normalized cross correlation. Proc SPIE 4387:95–102. https://doi.org/10.1117/12.421129
30. Pan C, Lv Z, Hua X, Li H (2020) The algorithm and structure for digital normalized cross-correlation by using first-order moment. Sensors 20(5):1353. https://doi.org/10.3390/s20051353
31. Lewis JP (1995) Fast normalized cross-correlation. In: Proceedings of Vision Interface pp. 120–123
32. Precitec GmbH (2025) CHRocodile 2S, https://www.precitec.com/optical-3d-metrology/products/point-sensors/chrocodile-2s/. [Accessed 1 Mar 2025].

Takeshi Hashimoto is currently a Ph.D. student in integrated design engineering at Keio University under the supervision of Prof. Jiwang Yan. His research interests include ultraprecision diamond turning of optics surfaces, machine tool design and control systems for ultraprecision machines. He also works for AMETEK Precitech Inc. as an application engineer.

Jiwang Yan received his Ph.D. from Tohoku University, Japan in 2000 and is currently a professor of Mechanical Engineering at KeioUniversity (2012-now), leading the Laboratory for Precision Machining and Nano Processing. His research areas include ultraprecision machining, micro/nano manufacturing, laser processing, nanomaterials, and nanomechanics.